Biophysical Journal
Article

Biophysical Society

Exploring the Membrane Potential of Simple Dual-Membrane Systems as Models for Gap-Junction Channels

Yerko Escalona,[1] Jose A. Garate,[1,4] Raul Araya-Secchi,[2] Tien Huynh,[3] Ruhong Zhou,[3] and Tomas Perez-Acle[1,4,*]
[1]Computational Biology Lab (DLab), Fundación Ciencia & Vida, Santiago, Chile; [2]Department of Chemistry and Biochemistry, The Ohio State University, Columbus, Ohio; [3]Computational Biology Center, IBM Thomas J. Watson Research Center, Yorktown Heights, New York; and [4]Centro Interdisciplinario de Neurociencia de Valparaíso (CINV), Universidad de Valparaíso, Valparaíso, Chile

ABSTRACT The conductance of ion channels can be modulated by a transmembrane potential difference, due to alterations on ion-mobility and also by changes in the pore structure. Despite the vast knowledge regarding the influence of voltage on transport properties of ion channels, little attention has been paid to describe, with atomic detail, the modulation of ionic transport in gap-junction channels (GJCs). Hence, molecular dynamics simulations were performed to explore the conductance of simple dual-membrane systems that account for the very basic features of GJCs. In doing so, we studied the influence of different charge distributions in the channel surface on these idealized systems under external electric fields, paying attention to the behavior of the electrostatic potential, ion density, ion currents, and equilibrium properties. Our results demonstrate that the incorporation of a charge distribution akin GJCs decreased anionic currents, favoring the transport of cationic species. Moreover, a thermodynamic characterization of ionic transport in these systems demonstrate the existence of a kinetic barrier that hinders anionic currents, reinforcing the role played by the internal arrangement of charges in GJCs. Overall, our results provide insights at the atomic scale on the effects of charge distributions over ionic transport, constituting a step forward into a better understanding of GJCs.

INTRODUCTION

As a result of the specific permeabilities of ionic species across the cell membrane, charge density is generally different on both the cytosolic and the extracellular reservoir. This heterogeneity of charge distribution is produced by the action of ionic pumps and ion channels (1), generating an electrochemical gradient, i.e., a voltage difference, which is crucial to regulate a variety of intercellular communication processes such as the regulation of cell homeostasis and the conduction of the neuron action potential (2). In the case of single-membrane systems, voltage-dependent modulation of ionic transport via structural rearrangements of ion channels is well understood, being extensively described by several groups with atomistic resolution (3–6). It depends on the presence of charged residues that will react under the influence of an external electrostatic potential, generating conformational changes to allow or disrupt the passage of ionic species through the channels. These channels communicate both the intracellular and the extracellular compartments, and they can also connect two adjacent cells by forming a so-called gap-junction channel (GJC) (7,8). GJCs connect the cytoplasm of adjacent cells to provide a dual-membrane hydrophilic channel between cells that enables the passive diffusion of water, ions, and small molecules. In detail, GJCs are composed by two opposed hemichannels (HCs) comprising six connexin (Cx) monomers (9–11). Experimental data has shown that the transport properties of GJCs are modulated by potential differences (12,13), demonstrating the existence of a voltage-regulated gating mechanism (14,15). Thus, GJCs are sensitive to voltages applied in different orientations: 1) the trans-membrane voltage, V_m, i.e., the voltage difference between the cytoplasm and the extracellular space; and 2) the transjunctional voltage, V_j, i.e., the voltage difference between the cytoplasm of the two adjacent cells. Considering their distinctive conductances, at least two distinct voltage-gating mechanisms have been identified in connexin channels: the loop or slow gating linked to the cytoplasmatic loop and C-terminal loop, and the fast gating, linked to residues

Submitted November 4, 2015, and accepted for publication May 3, 2016.
*Correspondence: tomas@dlab.cl
Yerko Escalona and Jose A. Garate contributed equally to this article.
Editor: Jose Faraldo-Gomez.
http://dx.doi.org/10.1016/j.bpj.2016.05.005

present at the N-terminal helix and the parahelix (a section of the first transmembrane helix, TM1) (13). Current evidence suggests that voltage-sensing residues are part of the pore because both opening and closing events are voltage-sensitive, thus the voltage sensors should be an integral part of the permeability barrier (12,16,17). Despite the accumulation of experimental evidence, the exact location, residue composition, and number of voltage sensors remain largely unknown (18). Within this context, a description, with atomic detail, of the effects of channel charge distributions under an external voltage over ion transport properties of GJCs, will shed lights on the role played by different pore-lining residues. However, few studies addressing this phenomena have been reported so far (19). Notwithstanding the fact that all-atom simulation approaches of similar macromolecular assemblies have been carried out (20,21), the understanding of the underlying mechanisms governing the behavior of these complex and large structures requires the development of simpler (and less computational demanding) model systems to evaluate working hypotheses. Following this approach, previous studies have shown that the basic features of voltage effects are preserved when employing simple pore models in molecular dynamics (MD) simulations, permitting an atomistic description of transport and structural properties, resulting voltages and thermodynamics (4,22–25).

In MD simulations, due to the (common) usage of periodic boundary conditions, the difference between both sides of a membrane disappears rendering a continuous bulk solution, thus no ionic gradient can be established. Several methods have been proposed to solve this issue. 1) Dual-membranes-dual-volumes or vacuum-slab-separated systems can generate the desired ionic asymmetry (26,27). 2) On the other hand, manual modification of the ionic concentrations can set the voltage to a desired value, although continuous adjustments during the simulation are required to maintain the voltage difference, especially when ionic species can permeate across the membranes (27). The latter can be alleviated by exchanging ions with water molecules employing a grand canonical Monte Carlo scheme (21). 3) More recently, the nonperiodic energy-step method was introduced (4); by applying a nonperiodic energy step to ionic species at the edge of the periodic box, realistic ionic asymmetries can be imposed and dynamically adjusted during the simulation. 4) Finally, an attractive and simple approach follows the application of a constant external electric field (E-field) along the desired direction, i.e., parallel to the membrane normal, as was first proposed by Crozier et al. (28). Later on, Aksimentiev and Schulten (29) laid the technical foundations of the E-field method by applying it to an ionic channel simulation, providing extensive validation and tool development for this methodology.

Herein, following the work of Gumbart et al. (25), we studied simplified dual-membrane systems as models for GJCs. These idealized and simplified models can be described as two rigid membranes composed of SP2 carbons with an inner pore that crosses two partitions. By applying the E-field method on MD simulations, a detailed description of resulting voltages and ionic properties (structural and dynamical) was obtained. Additionally, ionic permeation processes at equilibrium were investigated via potential of mean force (PMF) calculations. Overall, our results allowed us to rationalize the effects of internal charge distributions and voltage differences on ion transport in dual-membrane systems. Moreover, when a configuration of charges akin to GJCs was applied, anionic currents were reduced in accordance with the nonselective cationic preference of GJCs—a basic feature of these complex structures that lay at the heart of important intercellular communication processes such as the electrical synapsis.

MATERIALS AND METHODS

Model and GJC systems

Four model systems were constructed: a double membrane (2M), which is two membranes with two pores (2P); a single channel spanning two membranes (C); a single channel with explicit charges spanning two membranes with charges akin a GJC (which is a channel-bearing-explicit charges model, or CEC), and a single channel spanning two membranes with inverse charges (CEC_{inv}). Hydrophobic model membranes were constructed using individual SP2 carbons arranged in a body-centered cubic lattice with a spacing of 4 Å. Each membrane was composed of six vertical layers with a total thickness of 24 Å, with the dual membranes separated by a distance of 24 Å. For the pore-based systems (2P, C, CEC, and CEC_{inv}), a 20 Å-diameter hole was drilled out; the connecting channel was composed of a thin layer of individual carbon atoms. Additionally, the CEC model includes a charge distribution mimicking a GJC, with two rings with positive charges around the pore center and two rings with negative charges at the entrance of the channel. The CEC_{inv} exhibits the same geometric disposition but with inversed charges. Charges are 0.1 *e*. For the systems CECx2 and $CECx2_{inv}$, we double this value to 0.2 *e*. All systems were solvated and ionized with NaCl at a concentration of 300 mM in a periodic box of 48 × 48 × 128 Å, with each system consisting of ~22,000 atoms (see Fig. S1 in the Supporting Material and Figs. 1 and 2 for a schematic description of the simulated systems).

The all-atom GJC model was prepared from the 3.5 Å resolution x-ray crystal structure of Cx26, obtained from the Protein Data Bank (30), PDB: 2ZW3 (16). Missing atoms were added using the internal coordinates of the CHARMM (31) topology files, assuming pH 7.5 for protonation states; the protonation state of all histidines was chosen to be neutral according to the pK_a values predicted by PROPKA 3.0 (32). The dodecamer unit was constructed using two hemichannel models, each pertaining to six Cx26 monomers with completed loops using MODELER (33). The GJC dodecamer was embedded in two POPC lipid bilayers placed in the *x*-*y* plane using CHARMM GUI (34). Ions (Na^+, Cl^-) were randomly placed in the water to neutralize the system, reaching a final concentration of 150 mM. The final dimensions of the periodic cell were 142 × 142 × 215 Å, comprised of ~500,000 atoms (see Fig. 2 *A*). All systems were built using the program VMDv1.9 (35).

MD simulations

All simulations were performed with the MD program NAMDv2.9 (36) with the CHARMM 22 parameter set (31) and the TIP3P water model (37). A careful check at the Lennard-Jones parameters among the

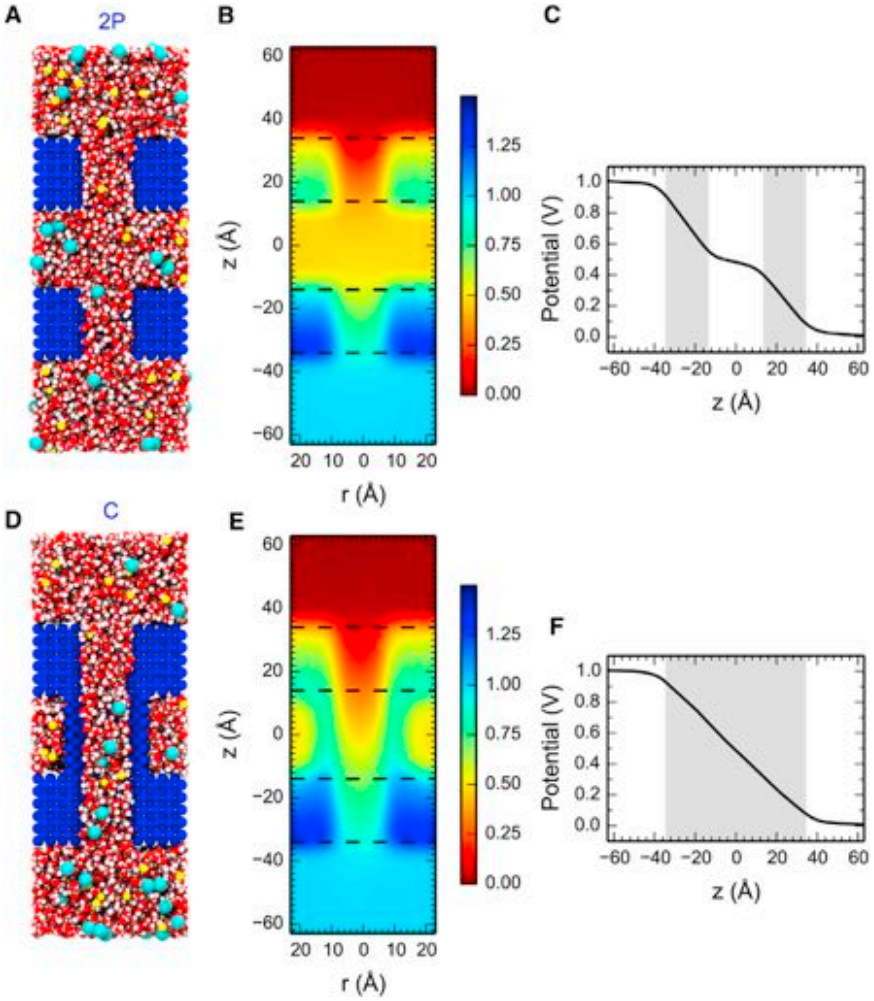

FIGURE 1 Average electrostatic potentials for the 2P and C models. All-atom molecular representation using van der Waals rendering of the 2P and the C models (*A* and *D*, respectively). Average electrostatic potentials along the *z* axis and the radial distance toward the pore center in the *x*-*y* plane, under an external potential of 1 V for the 2P and C models (*B* and *E*, respectively). (*C* and *F*) Average electrostatic potentials along the axial dimension under an external potential of 1 V for the 2P and C models. Dashed lines and shading, membrane(s) boundary(ies). To see this figure in color, go online.

aforementioned force field and the last version, CHARMM 36 (38), shows no substantial differences for the employed parameters. Briefly, the TIP3P water parameters are independent of any FF version; the SP2 carbons (C type) are equal, likewise the chloride ones (39); and only the CHARMM 36 sodium LJ parameter (as of January 2016) presents a slight increment in the $R_{min}/2$ parameter (4%).

The particle-mesh Ewald method (40) was used for full long-range electrostatics to within a relative tolerance of 1×10^{-6}. A cutoff distance of 12 Å was applied to real-space Ewald interactions. The same value was used for van der Waals interactions, with a smooth switching function applied thereto between 10 and 12 Å. Multiple time steps were used with 1 fs for bonded interactions, 1 fs for short-range nonbonded interactions, and 4 fs for the full electrostatics evaluation using the r-RESPA method (41). All production runs were performed coupled to an NVT reservoir, with a set point of 298 K using Langevin dynamics and a damping coefficient of 1 ps^{-1}. The SHAKE algorithm (42) was applied to constrain bond lengths to all hydrogen atoms, and the membrane atoms for the model systems were kept fixed during the simulations. Before production runs and as a way to avoid the dewetting of the hydrophobic carbon membranes, initial equilibration NPT runs were performed to fill out any possible cavities formed by the pseudo membrane; subsequently, any water molecule located within the membrane was removed.

In addition, MD simulations were run under the effects of an external static electric field (E-field). E-fields were applied with an intensity E of 0.180 Kcal mol^{-1} $Å^{-1}$ e^{-1} in the z axis, exerting a force over atomic partial charges q_{ia} defined by

$$f_{ia} = q_{ia}E_z, \tag{1}$$

where q stands for elementary charge units. The total potential across the periodic box for this E-field simply follows:

$$\Delta V_z = -E_z L_z, \tag{2}$$

with L_z standing for the z-axis length. Given the cell size and field strength, a rather large potential difference (1 V) was applied when compared to electrophysiological experiments (~−100 mV to 100 mV); the latter was deliberately designed to obtain meaningful data, i.e., ionic currents, in affordable simulation times 30 ns for the equilibrium simulations (without an electric field applied) and 100 ns to the nonequilibrium simulations (with an electric field applied).

Finally, the exploratory short MD simulations of the GJC explicit model were carried out as follows: an initial minimization and a short equilibration of 500 ps with a 0.5-fs time step were performed to allow the relaxation and accommodation of the system. Subsequently, a 20-ns equilibrium run was performed with the same parameters shown above for the hemichannel. After 20 ns, an external voltage of 1 V was imposed on the system for a 20-ns run. For this simulation, the damping coefficient was set to 1 ps^{-1} for the lipid heavy atoms only, and zero for all other atoms, thereby avoiding the spurious heating caused by E-fields and the artificial viscosity for bulk electrolytes introduced by the Langevin dynamics, as suggested in Sotomayor et al. (6).

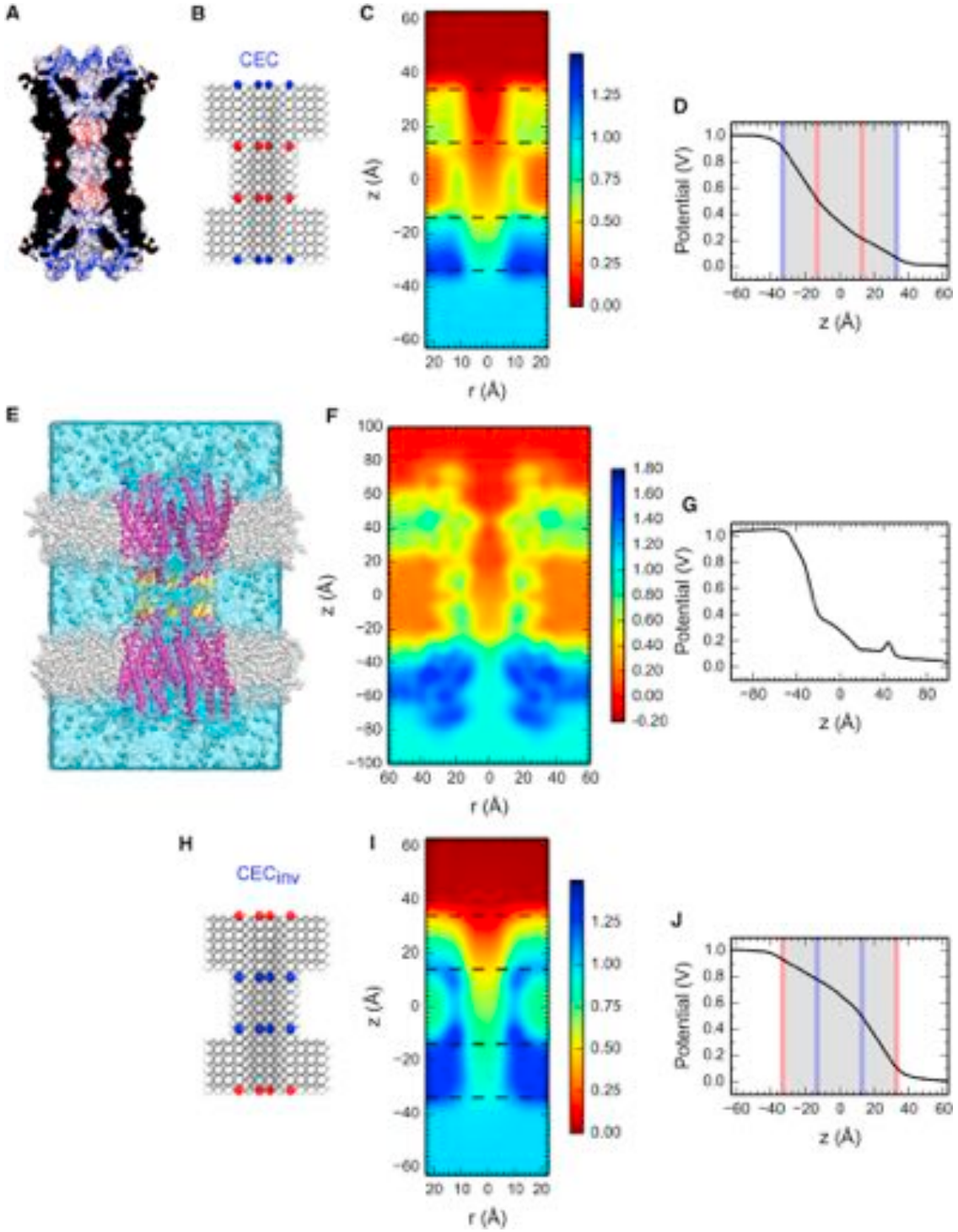

FIGURE 2 Average electrostatic potentials for the charges-bearing model systems and the hCx26 GJC. The electrostatic potential of the crystal structure of hCx26 (PDB: 2ZW3) (*A*). (*B* and *H*) Simplified representations of the CEC and CEC_{inv} model using van der Waals representation; only the channel and the charges (*blue*, positive; *red*, negative) are depicted. (*E*) All-atom molecular model of the hCx26 GJC embedded in a POPC membrane. (*C*, *F*, and *I*) Average electrostatic potentials along the *z* axis and the radial distance toward the pore center in the *x-y* plane, under an external potential of 1 V for the CEC, CEC_{inv}, and the hCx26 GJC models, respectively. (*D*, *G*, and *J*) Average electrostatic potentials along the *z* axis, under an external potential of 1 V for the CEC, CEC_{inv}, and the hCx26 GJC models, respectively. Dashed lines, membrane(s) boundary(ies); shading, charge placement. To see this figure in color, go online.

Electrostatic potentials

Electrostatic potentials were calculated employing the PME algorithm (40) via the PMEPOT plugin (29,35) from the VMD package (35). For simulations under an external E-field, the final potentials incorporate the PME potential, i.e., the reaction field, plus the linear potential resulting from Eq. 2. The electrostatics potentials were averaged over time after reaching steady state (generally, these were the last 30 ns of simulation time; for more

details, see Figs. S6 and S7) and along the x-y plane in the form axial (z axis)-radial profiles and in the form of axial profiles (see Figs. 1, 2, and S1–S4).

Ionic currents

Ionic currents across the periodic cell were computed by

$$I_{\text{avg}} = \lim_{t\to\infty} \frac{Q(t)}{t}, \tag{3}$$

where the electric charge ($Q(t)$) was computed by

$$Q(t) = \frac{1}{L_z} \sum_{\text{all atoms}} q_i[z_i(t) - z_i(0)], \tag{4}$$

where $z_i(t)$ represent the continuous unwrapped coordinates of the ith atom, L_z is the length of the periodic box along the z axis, and q_i stands for the charge of the ith ion (25).

Regarding the protocol utilized for ionic current calculations, all simulations were run to 100 ns. After reaching steady-state conditions, the last 50 ns were employed to compute average currents (see Fig. S6). The error was evaluated as the standard error.

Free-energy calculations

PMFs employing the metadynamics, local-elevation method (43,44), were carried out. In this work an extension of the metadynamics algorithm, well-tempered metadynamics (45) was employed with a precise formulation:

$$\mathcal{V}_{t+\delta t}(\boldsymbol{C_v}) = \mathcal{V}_t(\boldsymbol{C_v}) + W_0 e^{\frac{-\mathcal{V}_t(C_v)}{k_B \Delta T}} \prod_{i=1}^{N_{cv}} G(C_{vi}; d_i), \tag{5}$$

where $N_{cv}(\boldsymbol{C_v})$ is the dimensionality of free-energy projection (i.e., the number of collective variables C_{vi}, W_0, and d_i are free parameters—namely the height and bin width, respectively). G is a one-dimensional repulsive Gaussian "hill":

$$G(C_{vi}; d_i) = \exp\left(- \frac{(C_{vi}(q;t) - C_{vi}(q;t'))^2}{2\delta^2_{C_{vi}}} \right) \tag{6}$$

with centers located at previously visited configurations, extending by ~ $2\delta_{C_{vi}}$ along the C_{vi} direction. The latter depends parametrically on the bin width d_i. By reweighing the height of each Gaussian hill of Eq. 6, faster sampling and better convergence can be obtained (45); ΔT is a temperature-valued positive scalar parameter and $\mathcal{V}_t(\boldsymbol{C_v})$ is the bias energy for the collective variable space up to time t. In general, $\mathcal{V}(\boldsymbol{C_v})$ (for a sufficient long buildup time) is a good approximation of the negative of the PMF:

$$\text{PMF}(\boldsymbol{C_v}) \simeq -\frac{T + \Delta T}{\Delta T} \mathcal{V}(\boldsymbol{C_v})_{t\to\infty} + C, \tag{7}$$

where C is an arbitrary constant usually defined to set the lowest PMF to zero, and T is the simulations temperature, in this case 300 K.

In this work, the sodium and chloride passage processes were projected along two C_{vi}, the axial and radial distances from the periodic cell origin and toward the x-y plane center respectively, comprised of 212 × 12 grid points; the hill weight (W_0) was set to 0.1 Kcal/mol, with new hills added every 1000 time-steps (1 ps), and ΔT was set to 1200 K.

2D PMFs were integrated into one-dimensional PMFs employing the following expression:

$$\text{PMF}(z) = -k_B T \ln \left[\int_0^R dr \delta(z - z_0) e^{\text{PMF}(R,z)/k_B T} \right], \tag{8}$$

with $k_B T$ as the Boltzmann constant and T as the absolute temperature. From the 1D PMF profiles, the total free energies for an ion located at the bulk or in the pore can be computed by:

$$A_b = -k_B T \ln \left[\int_{\text{bulk}} e^{\text{PMF}(z)/k_B T} dz \right], \tag{9}$$

$$A_p = -k_B T \ln \left[\int_{\text{pore}} e^{\text{PMF}(z)/k_B T} dz \right], \tag{10}$$

where Eqs. 9 and 10 are integrated only for the bulk or pore regions, respectively. Finally the transfer energy from the bulk toward the pore is computed by

$$\Delta A^c_{b\to p} = A_p - A_b - k_B T \ln L_{zb} \frac{2\pi k_B T / k_{(xy)}}{V_b}, \tag{11}$$

where the last term in Eq. 11 is the ratio of the sampled unbound volume in the bulk ($L_{zb} 2\pi k_B T / k_{(xy)}$) when a harmonic restraint $k_{(xy)}$ is applied in the x-y plane, and the total bulk volume explored V_b (46). L_{zb} is the axial length of the bulk regions, and V_b is the total volume of the bulk region.

It is important to note that to improve convergence and reduce noise, i.e., avoid the formation of ions caps, PMF calculations were performed for systems containing a single ion (and its counterion) but, for diluted salt solutions and long simulations times, these two systems should converge toward similar results. Indeed, ionic density profiles obtained from both the CEC and CEC_{inv} simulations under zero E-field conditions (see Fig. S8) exhibit a good agreement with the PMF profiles of Fig. 4. Overall, convergence below thermal energy (~0.5 Kcal/mol at 298 K) was achieved for all PMF profiles; for more detail, see Figs. S10 and S11.

RESULTS AND DISCUSSION

Electrostatic potential of dual-membrane model systems

The validity and theoretical justification of the E-field method has been recently established (25,47). In practice, it represents a virtual circuit of two aqueous solutions held at a potential difference due to an electromotive force applied to the system of interest. Under this condition, a uniform aqueous-salt solution will reduce as much as possible the net electric field by inducing internal molecular rearrangements. Nonetheless, for nonuniform solutions, the self-organization of the bulk will generate a ubiquitous reaction field opposed to the external field; any potential drop can only localize within the zones where no such reaction field takes place, i.e., low-dielectric regions such as the cellular membrane (25,47). Therefore, to evaluate the effects on the resulting potential generated by the anisotropy of our models (see Materials and Methods), the electrostatic potentials for all simulated conditions were calculated as depicted in Figs. S1, 1, and 2.

In the simple dual-membrane system, the 2M (two membranes) model (Fig. S1), the potential only drops across the membranes, due to the lack of the reaction-field generated by the dipolar alignment of solvent molecules. In other words, the membranes act as an insulator. Furthermore, the potential difference across the simulation cell follows the linear regime expected from $V_z = -E_z L_z$ (25,47) with half-drops between each bulk reservoir.

The addition of pores to the 2M model renders the 2P (two pores) model (Fig. 1 *A*), allowing the diffusion of water and ions across the membranes that results in a reaction field given by the rearrangements of the confined particles. This rearrangement reduces the magnitude of the potential drop across the drilled insulator (see Fig. 1, *B* and *C*), separating the system in three iso-voltage regions. In the system where both pores are connected forming a channel, i.e., the C (channel) model (Fig. 1 *D*), the presence of the channel effectively splits the system into two regions, with only a single location (the channel) showing a linearized potential drop (see Fig. 1, *E* and *F*). These results confirm previous works that have demonstrated that the potential difference only depends on the periodic cell size and the magnitude of the applied field, and is insensitive to any microscopic detail (25). For completeness, the electrostatic potentials for all model systems under zero-field conditions are shown in Fig. S2.

Electrostatic potentials of the simplified GJC model

The prohibitive size of a full atomistic GJC model (>500 K atoms) restricts typical MD simulations to a couple of hundreds of nanoseconds, a simulation time that might be insufficient to obtain an equilibrated and fully open GJC, given its size and complexity. In fact, whether the only available crystal structure (hCx26) is in its open or closed conformation, is a matter of debate (16). To overcome the size limitation of the GJC, previous works have employed continuous electrostatics approximations in combination with Brownian dynamics (19). Nevertheless, these reduced descriptions partially or fully ignore the microscopic details of solvent molecules, which can lead to artifacts if those effects are not properly included. For this reason, a simplified dual-membrane model that accounts for the basic geometry and charge distribution of an open GJC, which explicitly includes solvent molecules, could draw a more faithful picture of these channels. In fact, following this approach, carbon nanotubes with modified charge distributions have been shown to qualitatively model water transport processes across aquaporin channels (23,48,49).

Electrophysiological experiments have demonstrated the voltage-dependent gating of GJCs; most of these channels show a transport behavior that is cation-non-specific (14,17,50). In agreement with other ion channels, this voltage-gating capability should be related to conformational changes occurring as a response to the external potential difference. Importantly, the cationic selectivity of these channels is mainly attributed to the asymmetries on its charge distribution (13,51). Each HC presents a polarity composed by positive charges in the intracellular side and negative charges flanking the extracellular side; indeed, this charge asymmetry mimics a P-N junction diode (51). Considering this evidence, to explore the microscopic repercussions that charge density has on ionic transport, we generated the CEC (channel-bearing-explicit charges) model, a system that explicitly includes charges to mimic the distribution of a GJC (see Fig. 2 *B*). Evidently, the nature of our rigid and simplified model only serves to assess cation selectivity but not voltage-dependent gating. However, its rigidity allows us to use higher voltages (1 V) to study the effects of charge configuration on ionic currents, isolating them from the effect of any conformational rearrangement.

The electrostatic potentials of the CEC model and a full-atomistic GJC model were qualitatively compared (see Materials and Methods for more details) as shown in Fig. 2, *C*, *D*, *F*, and *G*. As seen, the CEC model fairly reproduces the electrostatic potential of a GJC under a 1-V transmembrane potential difference; it rapidly drops in a concave exponential shape, exhibiting curves tilted toward lower potentials when compared to the neutral system (see Fig. 2, *D* and *G*). As expected, the complexity of the GJC model reduces the smoothness of the potential drop when compared to the CEC model, with a sharper drop due to the less insulating nature of the channel with the electrolytic solution between the membranes. The slight peak at the positive z axis (Fig. 2 *G*) is the result of a nonacetylated Lys, highlighting the importance of charge neutralization for ionic conductance as a result of posttranslational modifications in these channels (52). Consequently, to explore how the resulting potentials could be affected by a strong perturbation of the charge distribution, a model with inverted charges, the CEC_{inv} (channel bearing inverted explicit charges) model (Fig. 2 *H*), was further prepared. In this case, the potential drop is less sharp, exhibiting a convex exponential shape that is now symmetrically tilted toward higher potentials (see Fig. 2, *I* and *J*). The resulting symmetrical potentials under zero-field conditions (see Figs. S2 and S3) further justifies the validity of the CEC model. As a whole, our results confirm that the CEC model is able to roughly reproduce the electrostatics of a GJC. However, a thorough characterization of transport and thermodynamic properties of ionic passage must be performed, as it will be shown in the subsequent sections.

Ionic currents

Even though the total potential drop is not affected by the microscopic details of each unit cell (see above), transport properties of ionic species under an E-field will be

undoubtedly perturbed by both the particular geometry and charge distribution of the studied system. Consequently, we calculated average currents based on the electric charge by considering ion displacements through the unit cell throughout time (see Eq. 4 and Fig. S6), as shown in Table 1. As expected, under zero-field conditions, ionic currents tends to be zero; meanwhile, under a 1-V potential difference, total currents for the 2P and C systems differ by 18%, indicating that particle confinement actually plays a role. In fact, greater anionic currents are expected because chloride has a higher diffusion coefficient than sodium in TIP3P water (53). Interestingly, the presence of explicit charges significantly alter ionic currents; the CEC model induces an almost 30% reduction of the anionic current and an increase of 15% in the cationic current with respect to the C system. This behavior is in accordance with Harris and Locke (7), suggesting that charge distribution is an important factor rendering GJCs as nonspecific cationic channels. Indeed, available evidence suggests that the negative charges present in the first extracellular loop domain of Cx46 are responsible for ion selectivity (54). To further evaluate the role of charges as a key player in ion selectivity, we decided to produce a model with inverted charges—the CEC_{inv} model. Likewise, a reduction on cationic current was obtained (see Table 1). Nonetheless, this drop was close to 20% compared with the C model, with a 17% increase of the anionic current. Notably, chloride and sodium currents for both the CEC and CEC_{inv} models, respectively, are fairly similar. In other words, the strong electrostatic forces imposed by the presence of charges in the channel, essentially, compensate for any influence of the ion-intrinsic mobilities. An external bias of 0.5 V (50% less), as seen in Fig. S4, leads to similar results. In detail and assuming linear response (28), chloride current was reduced by 47% and sodium current presents an increment of 18% for the CEC model. On the other hand, the CEC_{inv} system generates no significant reduction in cationic current, with a 22% increment of anionic current (see Table 1). To further prove the role of the intrinsic charge distribution, extra simulations in which the charge distribution was doubled for both the CEC and the CEC_{inv} models, namely the CECx2 and CEC_{inv} x2 models, respectively, were carried out. As expected, the effects on ion mobility are intensified with respect to the C system; the CECx2 model shows a 62% reduction of anionic current under 1 V of transjunctional bias. Likewise, upon charge inversion, cationic currents are diminished by 48% (see Table S1).

A pictorial view of the aforementioned effects is achieved by plotting the average ionic densities along the simulated cell, as portrayed in Fig. 3. As seen, the 2P and C models contain a homogeneous distribution of ions with continuous chains along the channel (Fig. 3, *A* and *B*). On the other hand, when charges are present (Fig. 3, *C* and *D*), ionic density profiles suffer substantial changes exhibiting strong asymmetries, especially close to the pore mouths where ions tend to stack. The formation of the ionic caps is due to the particular charge arrangement of our models: for example, the CEC model, which possesses a positive charge density at the channel mouth and a negative charge density at the mid regions (see Fig. 2 *B*), enhances the presence of anions within the entrance of the upper and lower vestibules. The latter is observed in Fig. S8 *C*, in which higher anionic densities are present at the pore mouth for the CEC model under zero field conditions. A considerable free-energy barrier should hinder chloride penetration into the inner channel section, with minimums close to the channel entrance (see below). Accordingly, under a 1-V transjunctional bias, anions will enter through the $+z$ side, but due to the aforementioned free-energy barriers, these will tend to stack at the upper mouth, as observed in Fig. 3 *C*. On the contrary, the CEC_{inv} model favors anion location within the inner vestibule and given the field direction, chloride atoms will accumulate at the lower exit of it; i.e., $-z$ (see Fig. 3 *D*). An equivalent (symmetrically reversed) trend is observed for the sodium profiles.

Despite that the highest conductance of GJCs is achieved when the transjunctional voltage tends to zero (50)—evidence that on first sight will contradict the above results—this behavior is the result of a voltage-gating phenomena occurring in one of the HCs forming the GJC (17,55), a process that our simple models are not able to capture due to the lack of structural rearrangements under E-field conditions.

Permeation free-energy

The effective dynamics of permeating ions through biological channels is controlled by three factors: the PMF, the

TABLE 1 Ionic Currents for the Models Systems under Study

Current (*e*/ns)	Voltage (V)	2P	C	CEC	CEC_{inv}
Total	+1	2.90 ± 0.00	2.36 ± 0.00	2.02 ± 0.00	2.44 ± 0.00
Na^+	+1	1.12 ± 0.00	0.88 ± 0.00	1.00 ± 0.00	0.71 ± 0.00
Cl^-	+1	1.78 ± 0.00	1.48 ± 0.00	1.02 ± 0.00	1.73 ± 0.00
Total	+0.5	—	—	0.91 ± 0.00	1.32 ± 0.00
Na^+	+0.5	—	—	0.52 ± 0.00	0.43 ± 0.00
Cl^-	+0.5	—	—	0.39 ± 0.00	0.90 ± 0.00
Total	0	0.09 ± 0.00	−0.05 ± 0.00	0.01 ± 0.00	0.04 ± 0.00
Na^+	0	0.05 ± 0.00	0.01 ± 0.00	−0.04 ± 0.00	0.03 ± 0.00
Cl^-	0	0.05 ± 0.00	−0.06 ± 0.00	0.06 ± 0.00	0.01 ± 0.00

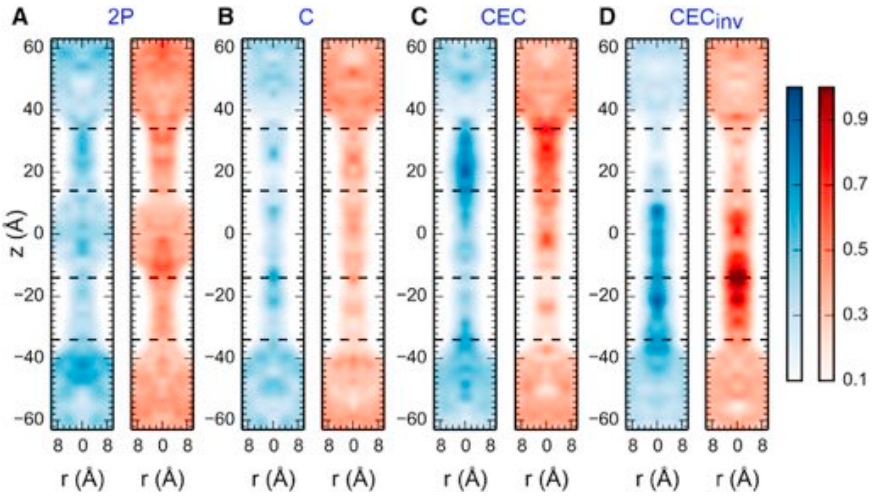

FIGURE 3 Average molar concentration of ions under an external voltage (1 V). The average molar concentration of ionic species (*blue*, sodium; *red*, chloride) as a function of the *z*-axis position and the radial distances toward the pore center in the *x*-*y* plane. In (*A*)–(*D*), the 2P, C, CEC, and CEC_{inv} models, respectively. Dashed lines, membrane contours. To see this figure in color, go online.

membrane potential, and the effective friction acting on the ions (25,56). Assuming that, in the context of our current simulation models, effective friction differences between the CEC and CEC_{inv} models are negligible, the main ingredients that will determine pore permeation are the membrane potential and its resulting PMF. In the previous sections we explored the effect of an E-field on ion currents; therefore, we decided to focus on the role of the PMF. In other words, we emphasize dissecting the intrinsic energetic barriers along the process of pore crossing. To do so, the free-energy landscape along a two-dimensional pathway (2D-PMF), i.e., the pore main axis and the radial distance to the pore center, was computed. The PMF is, of course, generated by an interplay between energetic and entropic effects. However, for monovalent ions, no rotational contribution exists and due to the strong charges present in both the CEC and CEC_{inv} models, diffusivity will be significantly hindered, thus discarding any gain in translational entropy. On the other hand, the energetic terms are mainly generated by Coulombic interactions, nonetheless for enclosed geometries (depending on the pore size) there might be a substantial cost due to the loss of the solvation shell. To explore this hypothesis, radial distribution functions for the water's oxygen, and both sodium and chloride, were determined. To do so, the integrity of the solvation shell upon pore infiltration by ions, was computed for the C model and compared to that of the bulk. As seen in Fig. S9, no differences regarding the radial distribution functions can be observed between the bulk and the C model for both ions. Therefore, any energetic penalty due to confinement is negligible for the channel radii considered here. Note that this penalty is likely significant for radii smaller than ~6 Å, where the ions must be desolvated to pass through the channel due to steric constraints (see Fig. S9). Once the role of confinement was ruled out (see above), the thermodynamics of the ion transport process was explored. We decided to compute 2D-PMFs for the passage of a single sodium and chloride ion across both the CEC and the CEC_{inv} models (see Fig. 4 and Materials and Methods for more details). For the sodium ion, the charge distribution of the CEC model generates a smooth profile with a unique minimum located at the pore center (see Fig. 4, *A* and *C*). Meanwhile, the CEC_{inv} model shifts the global minimum toward the bulk; however, despite symmetric considerations, this PMF presents a noticeable rugged profile with a noticeable barrier of ~4 Kcal/mol along the permeation pathway that will hinder the kinetics of the cation passage. For the strong voltages employed in this study (1 V), the work performed by the electric field (>7 Kcal/mol) fully overcomes the above barriers (see Fig. 4), explaining the occurrence of permeation events under E-field conditions and the small cationic current reduction for the CEC_{inv} model (see Table 1). Indeed, no permeation events were recorded for the zero-field simulations (data not shown). Consequently, the reduction of the chloride current for the CEC model follows the same arguments. Meanwhile, for the chloride ion, we observe the expected opposite effect with a preference toward the bulk in the CEC model (see Fig. 4, *E* and *G*) and with a unique minimum located at the pore center in the CEC_{inv} model (see Fig. 4, *F* and *H*). As a matter of fact, for a real GJC system a further reduction of anionic currents and increase of cationic currents can be assumed, given the expected more rugged PMF and lower physiological potential differences (~80 mV).

A 1-V bias is quite a strong potential with respect to physiological relevant voltages, e.g., 0.1 V, but our systems are rigid—thus any perturbation due to conformational flexibility or electroporation processes is discarded. Moreover, many of these effects require timescales that are beyond the length of our simulations. Nevertheless, such a strong force could render very short-termed ion-pore interactions. This was the main reason to perform the PMF calculations in the absence of any external voltage; in this form, we were able to capture the equilibrium thermodynamics of the ionic permeation process. Indeed, the existence of anionic or cationic currents for the CEC and CEC_{inv}, respectively, at

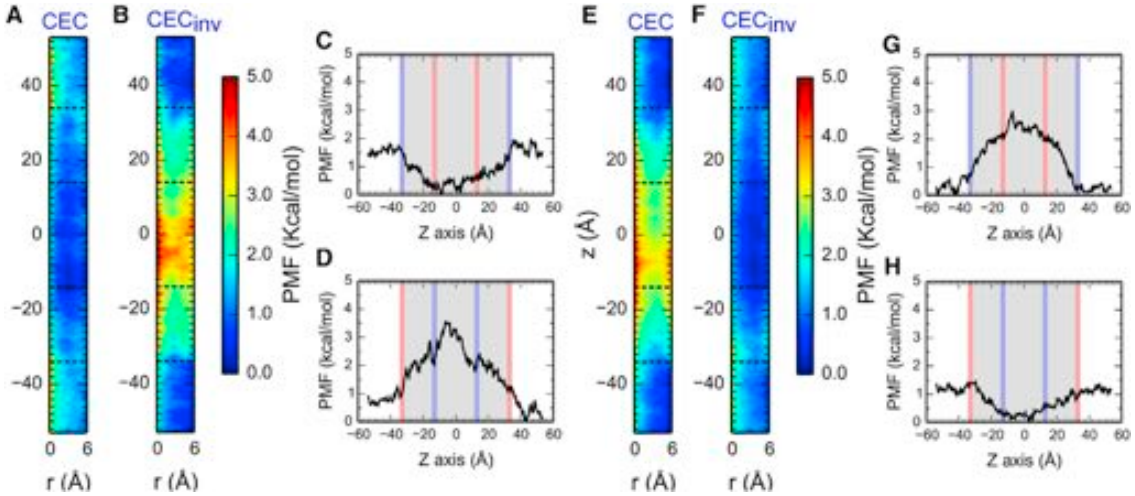

FIGURE 4 PMFs of ion permeation. PMF profiles for the sodium (*A–D*) and chloride (*E–G*) permeation processes. 2D-PMF profiles for the sodium permeation process projected along the *z* axis and the radial distance toward the pore center in the *x-y* plane, for the CEC (*A*) and CEC$_{inv}$ (*B*) models. 1D-PMF profiles for the sodium permeation process projected along the *z* axis, for the CEC (*C*) and CEC$_{inv}$ (*D*) models. 2D-PMF and 1D-PMF profiles for the chloride permeation for the CEC (*E* and *G*) and CEC$_{inv}$ (*F* and *H*) models. Shaded spanning region, position of the membranes; dashed lines, membrane contours. To see this figure in color, go online.

1 V (see Table 1), even though the presence of free energy barriers above thermal noise, i.e., ≈0.5 Kcal/mol (see Fig. 4), is a clear evidence of the strong employed bias.

For completeness, the integrated transfer free-energy differences from the bulk toward the channel for all models, before ($\Delta A_{b\to p}$, first column of Table 2) and after ($\Delta A^{c}_{b\to p}$, second column of Table 2) applying the corresponding volumetric corrections (see Eq. 11), are shown in Table 2 (see also Fig. S10 for the PMF profiles of the 2P and C models). Briefly, the entropic penalty due to confinement renders all transfers a nonspontaneous process. Nonetheless, the exerted work by the applied voltages fully overcomes the values shown in Table 2, as explained above.

CONCLUSIONS

Ionic currents through biological channels are modulated by the PMFs of permeation, the membrane potential, and the effective friction acting on transported ions (25,56). In particular, in voltage-dependent ion channels such as GJCs, these currents are sensitive to the existence of a potential difference across the membrane (12–15). GJCs can be modulated by voltage, acting as rectifying ion channels exhibiting voltage-dependent gating (50). While the former property is related to asymmetries in charge distributions within the channel, the latter depends on conformational changes promoted by the existence of a transmembrane potential difference (13). Numerous studies based on MD simulations of single-membrane ion channels have characterized the effect of transmembrane potential (3–6). However, to our knowledge, no studies have been focused on the effects of the intrinsic (pore-lining) charge density under voltage differences on dual-membrane molecular systems.

In this way, we developed a set of simple dual-membrane setups as models for GJCs. As expected, our results show that the potential drop in the 2P model exhibits a linear decay at the membrane location (Fig. 1 *C*). A similar tendency is observed when a channel connects both membranes in the C model (Fig. 1 *F*). Therefore, when no charges are present in our models, both decays follow the linear regime expected from $V_z = -E_z L_z$ (25,47). With the introduction of charges to our models, i.e., the CEC and the CEC$_{inv}$ models, the potential drop is dramatically changed in accordance to the nature of the charges introduced to the systems (Fig. 2). In detail, a charge configuration akin to a GJC (the CEC model) exhibits a potential drop that follows an exponential decay (Fig. 2 *G*). On the contrary, when charges were inverted, the potential drop exhibits a convex shape (Fig. 2 *J*). Ion current calculations (Table 1) revealed that the CEC model exhibits an enhancement of cationic current with respect to the C model. Meanwhile, when charges were inverted to produce the CEC$_{inv}$ model, the channel presents a higher anionic current with respect to the C model. In this manner, the intrinsic charge distribution of GJCs is a

TABLE 2 Transfer Free Energies

System (Ion)	$\Delta A_{b\to p}$ [a]	$\Delta A^{c}_{b\to p}$ [b]
2P (Na^+)	0.12 ± 0.03	3.48 ± 0.03
C (Na^+)	0.27 ± 0.03	3.65 ± 0.03
CEC (Na^+)	−0.99 ± 0.03	2.38 ± 0.03
CEC$_{inv}$ (Na^+)	0.92 ± 0.07	4.29 ± 0.07
CEC (Cl^-)	0.71 ± 0.07	4.09 ± 0.07
CEC$_{inv}$ (Cl^-)	−0.80 ± 0.03	2.57 ± 0.03

[a]Raw free energy ($\Delta A_{b\to p} = A_p - A_b$).
[b]Corrected free energy (see Eq. 11).

key element for ion selectivity, as suggested before (54,57,58).

The PMF calculations (Fig. 4) of sodium passage confirmed the previous results. For the CEC model, the PMF profile is relatively flat, with a global minimum at the channel center, favoring cation selectivity. On the other hand, the height of the PMF at the central region of the CEC_{inv} model, translates into a kinetic barrier, in full accordance with the cationic current reduction reinforcing the role played by negative internal charges on GJCs. The chloride PMFs further proved the influence of the intrinsic GJC charge distribution, with symmetrically reversed results with respect to the sodium profiles.

Overall, these somewhat simplified dual-membrane models offer a clear molecular picture with atomistic detail of more complex phenomena occurring in GJCs. Despite their simplicity, which does not encompass any structurally mediated voltage-gating mechanism, they offer a fertile landscape for the understanding of the role of charge distribution within GJCs and the resulting voltages when an external E-field is applied.

SUPPORTING MATERIAL

Supporting Materials and Methods, eleven figures, and one table are available at http://www.biophysj.org/biophysj/supplemental/S0006-3495(16)30281-8.

AUTHOR CONTRIBUTIONS

Y.E. and J.A.G. equally contributed to the article; Y.E., J.A.G., R.A.-S., R.Z., and T.P.-A. designed research; Y.E., R.A.-S., and T.H. performed molecular simulations; all authors discussed and analyzed the data; Y.E., J.A.G., and T.P.-A. wrote the main article; and R.A.-S., T.H., and R.Z. wrote and revised the article.

ACKNOWLEDGMENTS

The authors acknowledge suggestions, comments, and guidance provided by Marcos Sotomayor. Y.E. acknowledges comments from Alejandro Bernardin and Sebastian Gutierrez. Y.E. acknowledges Octavio Monasterio for his support.

This work was partially supported by grant No. PFB16 Fundación Ciencia para la Vida; ICM-Economía grant No. P09-022-F Centro Interdisciplinario de Neurociencia de Valparaíso, Universidad de Valparaíso; FONDECYT grant No. 1160574 (to T.P.A.); and FONDECYT grant No. 3130547 (to J.A.G.). Access to the supercomputing infrastructure of the National Laboratory for High Performance Computing was supported through grant No. ECM-02 (Powered@NLHPC). R.Z. acknowledges support from the IBM Blue Gene Science Program.

REFERENCES

1. Hille, B. 2001. Ion Channels of Excitable Membranes, 3rd Ed. Sinauer Associates, Sunderland, MA.
2. Bezanilla, F. 2008. How membrane proteins sense voltage. *Nat. Rev. Mol. Cell Biol.* 9:323–332.
3. Groome, J. R. 2014. The voltage sensor module in sodium channels. *Handbook Exp. Pharmacol.* 221:7–31.
4. Khalili-Araghi, F., B. Ziervogel, …, B. Roux. 2013. Molecular dynamics simulations of membrane proteins under asymmetric ionic concentrations. *J. Gen. Physiol.* 142:465–475.
5. Villinger, S., R. Briones, …, M. Zweckstetter. 2010. Functional dynamics in the voltage-dependent anion channel. *Proc. Natl. Acad. Sci. USA.* 107:22546–22551.
6. Sotomayor, M., V. Vásquez, …, K. Schulten. 2007. Ion conduction through MscS as determined by electrophysiology and simulation. *Biophys. J.* 92:886–902.
7. Harris, A. L., and D. Locke. 2009. Connexins: a Guide. Humana Press, Totowa, NJ.
8. Meşe, G., V. Valiunas, …, T. W. White. 2008. Connexin26 deafness associated mutations show altered permeability to large cationic molecules. *Am. J. Physiol. Cell Physiol.* 295:C966–C974.
9. Yeager, M., and N. B. Gilula. 1992. Membrane topology and quaternary structure of cardiac gap junction ion channels. *J. Mol. Biol.* 223:929–948.
10. Yeager, M. 1998. Structure of cardiac gap junction intercellular channels. *J. Struct. Biol.* 121:231–245.
11. Saez, J. C., V. M. Berthoud, …, E. C. Beyer. 2003. Plasma membrane channels formed by connexins: their regulation and functions. *Physiol. Rev.* 83:1359–1400.
12. Ek-Vitorin, J. F., and J. M. Burt. 2013. Structural basis for the selective permeability of channels made of communicating junction proteins. *Biochim. Biophys. Acta.* 1828:51–68.
13. Oh, S., and T. A. Bargiello. 2015. Voltage regulation of connexin channel conductance. *Yonsei Med. J.* 56:1–15.
14. Harris, A. L., D. C. Spray, and M. V. Bennett. 1981. Kinetic properties of a voltage-dependent junctional conductance. *J. Gen. Physiol.* 77:95–117.
15. Spray, D. C., A. L. Harris, and M. V. Bennett. 1981. Equilibrium properties of a voltage-dependent junctional conductance. *J. Gen. Physiol.* 77:77–93.
16. Maeda, S., S. Nakagawa, …, T. Tsukihara. 2009. Structure of the connexin 26 gap junction channel at 3.5 Å resolution. *Nature.* 458:597–602.
17. Bukauskas, F. F., and V. K. Verselis. 2004. Gap junction channel gating. *Biochim. Biophys. Acta.* 1662:42–60.
18. Araya-Secchi, R., T. Perez-Acle, …, R. Zhou. 2014. Characterization of a novel water pocket inside the human Cx26 hemichannel structure. *Biophys. J.* 107:599–612.
19. Kwon, T., A. L. Harris, …, T. A. Bargiello. 2011. Molecular dynamics simulations of the Cx26 hemichannel: evaluation of structural models with Brownian dynamics. *J. Gen. Physiol.* 138:475–493.
20. Hub, J. S., C. Aponte-Santamaría, …, B. L. de Groot. 2010. Voltage-regulated water flux through aquaporin channels in silico. *Biophys. J.* 99:L97–L99.
21. Kutzner, C., H. Grubmüller, …, U. Zachariae. 2011. Computational electrophysiology: the molecular dynamics of ion channel permeation and selectivity in atomistic detail. *Biophys. J.* 101:809–817.
22. Li, J., X. Gong, …, R. Zhou. 2007. Electrostatic gating of a nanometer water channel. *Proc. Natl. Acad. Sci. USA.* 104:3687–3692.
23. Garate, J. A., N. English, and J. MacElroy. 2009. Carbon nanotube assisted water self-diffusion across lipid membranes in the absence and presence of electric fields. *Mol. Simul.* 35:3–12.
24. Garate, J. A., N. J. English, and J. M. D. MacElroy. 2009. Static and alternating electric field and distance-dependent effects on carbon nanotube-assisted water self-diffusion across lipid membranes. *J. Chem. Phys.* 131:114508.
25. Gumbart, J., F. Khalili-Araghi, …, B. Roux. 2012. Constant electric field simulations of the membrane potential illustrated with simple systems. *Biochim. Biophys. Acta.* 1818:294–302.

26. Sachs, J. N., P. S. Crozier, and T. B. Woolf. 2004. Atomistic simulations of biologically realistic transmembrane potential gradients. *J. Chem. Phys.* 121:10847–10851.

27. Delemotte, L., F. Dehez, …, M. Tarek. 2008. Modeling membranes under a transmembrane potential. *J. Phys. Chem. B.* 112:5547–5550.

28. Crozier, P. S., D. Henderson, …, D. D. Busath. 2001. Model channel ion currents in NaCl-extended simple point charge water solution with applied-field molecular dynamics. *Biophys. J.* 81:3077–3089.

29. Aksimentiev, A., and K. Schulten. 2005. Imaging α-hemolysin with molecular dynamics: ionic conductance, osmotic permeability, and the electrostatic potential map. *Biophys. J.* 88:3745–3761.

30. Berman, H. M., J. Westbrook, …, P. E. Bourne. 2000. The Protein Data Bank. *Nucleic Acids Res.* 28:235–242.

31. MacKerell, A. D. J., D. Bashford, …, M. Karplus. 1998. All-atom empirical potential for molecular modeling and dynamics studies of proteins. *J. Phys. Chem. B.* 102:3586–3616.

32. Olsson, M. H. M., C. R. Søndergaard, …, J. H. Jensen. 2011. PROPKA3: consistent treatment of internal and surface residues in empirical pK_a predictions. *J. Chem. Theory Comput.* 7:525–537.

33. Sali, A., and T. L. Blundell. 1993. Comparative protein modelling by satisfaction of spatial restraints. *J. Mol. Biol.* 234:779–815.

34. Jo, S., J. B. Lim, …, W. Im. 2009. CHARMM-GUI Membrane Builder for mixed bilayers and its application to yeast membranes. *Biophys. J.* 97:50–58.

35. Humphrey, W., A. Dalke, and K. Schulten. 1996. VMD: visual molecular dynamics. *J. Mol. Graph.* 14:33–38, 27–28.

36. Phillips, J. C., R. Braun, …, K. Schulten. 2005. Scalable molecular dynamics with NAMD. *J. Comput. Chem.* 26:1781–1802.

37. Jorgensen, W. L., J. Chandrasekhar, …, M. L. Klein. 1983. Comparison of simple potential functions for simulating liquid water. *J. Chem. Phys.* 79:926.

38. Klauda, J. B., R. M. Venable, …, R. W. Pastor. 2010. Update of the CHARMM all-atom additive force field for lipids: validation on six lipid types. *J. Phys. Chem. B.* 114:7830–7843.

39. Beglov, D., and B. Roux. 1994. Finite representation of an infinite bulk system: solvent boundary potential for computer simulations. *J. Chem. Phys.* 100:9050–9063.

40. Darden, T., D. York, and L. Pedersen. 1993. Particle mesh Ewald: an N log(N) method for Ewald sums in large systems. *J. Chem. Phys.* 98:10089.

41. Tuckerman, M., B. Berne, and G. Martyna. 1992. Reversible multiple time scale molecular dynamics. *J. Chem. Phys.* 97:1990–2001.

42. Ryckaert, J.-P., G. Ciccotti, and H. J. Berendsen. 1977. Numerical integration of the Cartesian equations of motion of a system with constraints: molecular dynamics of *n*-alkanes. *J. Comput. Phys.* 23: 327–341.

43. Huber, T., A. E. Torda, and W. F. van Gunsteren. 1994. Local elevation: a method for improving the searching properties of molecular dynamics simulation. *J. Comput. Aided Mol. Des.* 8:695–708.

44. Laio, A., and M. Parrinello. 2002. Escaping free-energy minima. *Proc. Natl. Acad. Sci. USA.* 99:12562–12566.

45. Barducci, A., G. Bussi, and M. Parrinello. 2008. Well-tempered metadynamics: a smoothly converging and tunable free-energy method. *Phys. Rev. Lett.* 100:020603.

46. Doudou, S., N. A. Burton, and R. H. Henchman. 2009. Standard free energy of binding from a one-dimensional potential of mean force. *J. Chem. Theory Comput.* 5:909–918.

47. Roux, B. 2008. The membrane potential and its representation by a constant electric field in computer simulations. *Biophys. J.* 95:4205–4216.

48. Zhu, F., and K. Schulten. 2003. Water and proton conduction through carbon nanotubes as models for biological channels. *Biophys. J.* 85:236–244.

49. Zuo, G., R. Shen, …, W. Guo. 2010. Transport properties of single-file water molecules inside a carbon nanotube biomimicking water channel. *ACS Nano.* 4:205–210.

50. Harris, A. L. 2001. Emerging issues of connexin channels: biophysics fills the gap. *Q. Rev. Biophys.* 34:325–472.

51. Oh, S., V. K. Verselis, and T. A. Bargiello. 2008. Charges dispersed over the permeation pathway determine the charge selectivity and conductance of a Cx32 chimeric hemichannel. *J. Physiol.* 586:2445–2461.

52. D'hondt, C., J. Iyyathurai, …, G. Bultynck. 2013. Regulation of connexin- and pannexin-based channels by post-translational modifications. *Biol. Cell.* 105:373–398.

53. Joung, I. S., and T. E. Cheatham, 3rd. 2009. Molecular dynamics simulations of the dynamic and energetic properties of alkali and halide ions using water-model-specific ion parameters. *J. Phys. Chem. B.* 113:13279–13290.

54. Trexler, E. B., F. F. Bukauskas, …, V. K. Verselis. 2000. The first extracellular loop domain is a major determinant of charge selectivity in connexin46 channels. *Biophys. J.* 79:3036–3051.

55. Oh, S., C. K. Abrams, …, T. A. Bargiello. 2000. Stoichiometry of transjunctional voltage-gating polarity reversal by a negative charge substitution in the amino terminus of a connexin32 chimera. *J. Gen. Physiol.* 116:13–31.

56. Roux, B., T. Allen, …, W. Im. 2004. Theoretical and computational models of biological ion channels. *Q. Rev. Biophys.* 37:15–103.

57. Xin, L., X.-Q. Gong, and D. Bai. 2010. The role of amino terminus of mouse Cx50 in determining transjunctional voltage-dependent gating and unitary conductance. *Biophys. J.* 99:2077–2086.

58. Tong, X., H. Aoyama, …, D. Bai. 2014. Charge at the 46th residue of connexin 50 is crucial for the gap-junctional unitary conductance and transjunctional voltage-dependent gating. *J. Physiol.* 592:5187–5202.